

Structural basis of PANX1 permeation and positive modulation by mefloquine

Received: 18 September 2025

Accepted: 25 October 2025

Published online: 11 December 2025

 Check for updates

Yangyang Li^{1,7}, Zheng Ruan  ^{2,5,7}, Junuk Lee¹, Ian J. Orozco^{2,6}, Edward Zhou¹, Juan Du  ^{1,2,3,4}  & Wei Lü  ^{1,2,3,4} 

Purinergic signaling relies on ATP release through exocytosis and large-pore channels. Large-pore channels permeate both small anions like chloride and large signaling molecules like ATP, but how this broad cargo selectivity is structurally controlled remains elusive. Here we investigate PANX1, a prototypical large-pore channel, and uncover structural plasticity at the extracellular entrance formed by seven tryptophan (W74) residues. The W74 sidechains are flexible, sampling conformations that range from a constricted state permissive only to chloride to a dilated state compatible with ATP. These states are coupled to variable cation–π interactions between W74 and arginine 75 (R75), suggesting a mechanism for dynamic tuning of pore architecture and selective cargo permeation. We also identify mefloquine as a positive modulator of PANX1 that binds near the side tunnel to control ion flow through this pathway. Together, these findings define the structural principles underlying PANX1 permeation and modulation.

Purinergic signaling is a critical and versatile cell communication system in the body that involves the release, detection, and response to signaling molecules such as adenosine triphosphate (ATP) or its derivates¹. It has a wide range of physiological and pathological implications including taste perception, neuronal inflammation, synaptic plasticity, and muscle development^{2–5}. ATP release into the extracellular environment marks the initial step of this pathway, predominantly facilitated by exocytosis⁶ or ATP-release channels such as connexin, pannexin, volume-regulated anion channels, and calcium homeostasis modulators⁴. These channels, characterized by their large pore sizes compared to the conventional ion channels, allow the passage of both small ions like chloride and large cellular metabolites like ATP⁷. However, the fundamental question of how these channels accommodate entirely different cargo molecules for permeation remains elusive, as obtaining structural information on large-pore channel with clearly defined functional states proved difficult. Furthermore, targeting large-pore channels presents a major challenge due to the scarcity of known druggable sites, primarily confined to the

extracellular restriction site, at which inhibitors are known to block channel activity⁷. These channel blockers, however, lack selectivity across different large-pore channel families. The exploration of new drug binding sites, including those for positive allosteric modulators that enhance channel function, remains an ongoing endeavor.

Pannexin 1 (PANX1) has garnered substantial attention as a relatively well-studied large-pore channel, owing to its important role in various physiological processes, including immune response, cardiac development, apoptosis, and synapse function^{8–11}. Inhibiting PANX1 has shown promise in mitigating oocyte degeneration during in vitro fertilization¹². Extensive structural and functional studies reveal PANX1 as a heptameric complex with a main pore in the center responsible for cargo transport (Fig. 1a)^{13–20}. The intracellular opening of the main pore is physically blocked by the C-terminal tail (CTT) domain. Caspase 3/7 cleavage of the CTT domain irreversibly activates the channel to release ATP, which, in turn, triggers phagocytosis to clear dying cells^{21,22}. The extracellular restriction site of the main pore is notably open in the published PANX1 structures, with a diameter of ~8 Å.

¹Department of Molecular Biosciences, Northwestern University, Evanston, IL, USA. ²Department of Structural Biology, Van Andel Institute, Grand Rapids, MI, USA. ³Department of Pharmacology, Northwestern University, Feinberg School of Medicine, Chicago, IL, USA. ⁴Chemistry of Life Processes Institute, Northwestern University, Evanston, IL, USA. ⁵Present address: Department of Biochemistry & Molecular Biology, Thomas Jefferson University, Philadelphia, PA, USA. ⁶Present address: AnaBios Corporation, San Diego, CA, USA. ⁷These authors contributed equally: Yangyang Li, Zheng Ruan.

 e-mail: juan.du@northwestern.edu; wei.lu@northwestern.edu

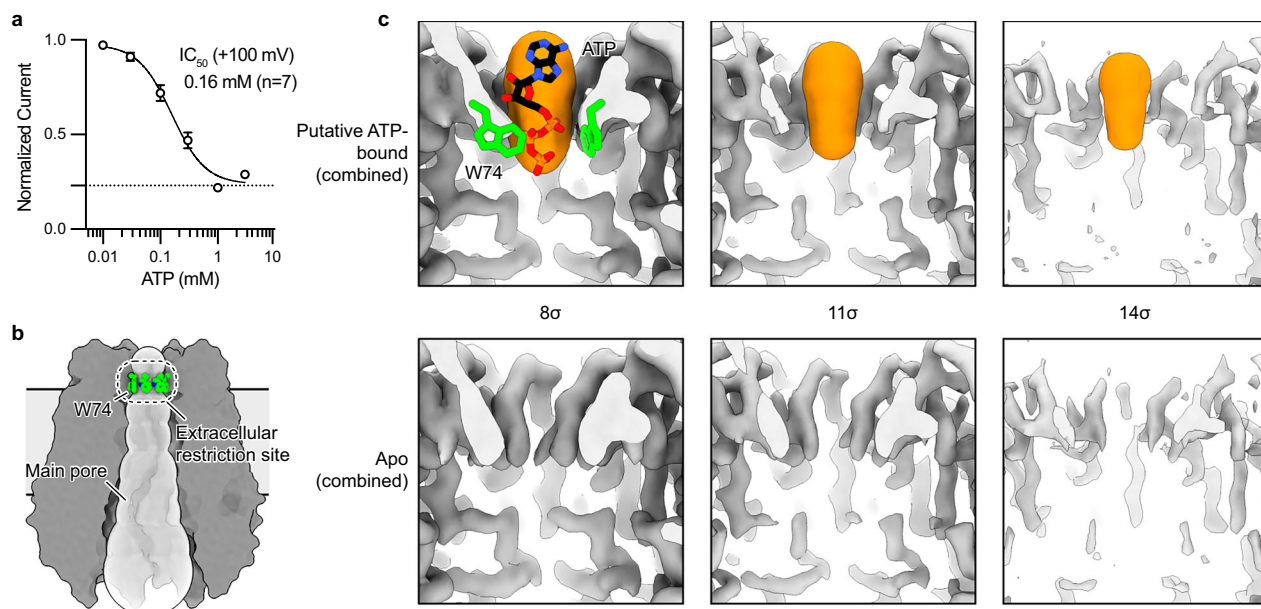


Fig. 1 | Putative ATP density at the extracellular restriction site of PANX1.

a Dose-response curve showing ATP partially inhibits PANX1, with n indicating the number of independent cells recorded in whole-cell patch clamp experiments. **b** Slice view of the PANX1 atomic model, oriented parallel to the membrane, with the main ion-conducting pore shown as a semitransparent tube. The extracellular

restriction site is formed by seven W74 residues (shown in green). **c** Close-up views of the extracellular restriction site in the putative ATP-bound (combined) cryo-EM map (top row) and the apo (combined) map, contoured at the indicated sigma levels. Putative ATP densities are shown in orange. ATP and the side chains of W74 from two subunits are shown in stick representation.

Whether this pore size represents an active/open or inactive/closed state for ATP release remains debated, as it is smaller than the hydrated diameter of ATP (~12 Å)^{23,24}. However, the possibility for ATP to undergo dehydration before permeation should not be dismissed—the size of a dehydrated ATP seems compatible with the extracellular restriction site—particularly considering the hydrophobic nature of the W74 residue that constitutes the extracellular restriction site. Moreover, the suggestion that the extracellular domain (ECD) of PANX1 may undergo substantial conformational changes to facilitate ATP permeation appears to contrast with the seemingly rigid structure of the ECD^{13,24}.

In addition to the main pore, we previously identified seven side tunnels between neighboring subunits in PANX1¹³. These side tunnels run roughly parallel to the cell membrane along the surface of the cytoplasmic leaflet, bypassing the CTT blockage and ultimately connecting to the main pore, with which they share the extracellular exit¹³. The side tunnels contribute to ionic conductance of PANX1, particularly under nonapoptotic conditions. Mutations that expand or shrink the side tunnels correspondingly enhance or attenuate the side tunnel conductance¹³. Intriguingly, gain-of-function variants in PANX1 that potentiate the side tunnel conductance have been directly linked to oocyte death and female infertility¹². Considering the conserved arrangement of the transmembrane structural domain (TMD) among large-pore channels, side tunnels are theoretically present across these channels, albeit with distinct amino acid compositions. This unique property makes the modulation of side tunnels, in contrast to modulation of the extracellular restriction site, a promising avenue, holding great potential for the development of selective drugs targeting large-pore channels.

Given the physiological importance of ATP permeation and the pathological importance of manipulating PANX1 activity for the treatment of various diseases, here we investigate human PANX1 by combining single-particle cryo-EM, patch-clamp electrophysiology, and computational simulation, aiming to elucidate the mechanism underlying the permeation of both small anions and large cellular metabolites, as well as the pharmacological modulation of PANX1.

Results

ATP-dependent density at the extracellular pore entrance

The release of ATP via large-pore channels initiates purinergic signaling; however, the underlying molecular mechanism has remained elusive. This is largely due to the challenge of capturing structural snapshots of large-pore channels in complex with their cargo, ATP, and these snapshots are necessary to determine the permeation pathway as well as to define conformational changes that gate the channel. Interestingly, apart from being a cargo molecule for the PANX1 channel, excessive extracellular ATP also exhibits a blocking effect on PANX1 channel activity. However, the blocking effect is modest, as evidenced by an IC_{50} in the submillimolar range, and the observation that even saturating extracellular ATP inhibited PANX1 by only ~75% (Fig. 1a)²⁵. The dual roles of ATP provide an opportunity to capture the ATP-bound complex structure at millimolar ATP concentrations. However, a major challenge in assessing ATP binding lies in the presence of endogenous metabolites—ATP included—that may remain associated with the protein even after purification, particularly given that PANX1 is permeable to a range of cellular metabolites and ions of comparable size. This is a known complication in structural studies of membrane proteins, as endogenous ligands may dissociate very slowly once removed from the native lipid environment²⁶, making it difficult to determine whether any observed ligand density originates from the added ligand or from residual endogenous sources.

To mitigate this, we implemented an extensive dialysis step of the membrane fraction prior to detergent solubilization (see Methods), aimed at reducing residual binding of endogenous ligands. We then purified PANX1 and prepared cryo-EM grids either without added ATP (0 mM ATP) or under defined saturating ATP concentrations (10, 20, and 30 mM), ensuring all samples were derived from the same preparation. This strategy enabled a controlled comparison of ligand-binding states. With these preparations, high-quality structures with similar resolutions were obtained under each condition, with resolutions ranging from 2.6 to 2.7 Å (Supplementary Table 1; and Supplementary Figs. 1, 2). The uniform quality and resolution of these data

provide a solid foundation for assessing both ATP occupancy and the conformational dynamics of the protein.

Although an extra density within the extracellular restriction site was observed in all four datasets without and with ATP, it appeared weak without added ATP but became more pronounced under ATP-supplemented conditions (Supplementary Fig. 3a). This suggests that the density is related to the added ATP, possibly representing bound ATP. We did not observe any evidence of ATP binding elsewhere in the protein, despite the high quality of the maps. However, even under saturating ATP concentrations, the density remained featureless cylindrical and shorter than an ATP molecule (Supplementary Fig. 3a)—possibly reflecting partial occupancy or a dynamic ensemble of ATP poses averaged during reconstruction.

Pore-blocked and apo states of PANX1 resolved from ATP-added samples

To better understand the pore-blocking density, we developed a reproducibility-guided focused classification framework to resolve conformational heterogeneity at the extracellular restriction site and distinguish putative ATP-bound state from ATP-free apo state (see Methods, Supplementary Fig. 3b and Supplementary Table 2). This approach proved effective, as it revealed distinct 3D classes—some displaying a strong pore-blocking density, others entirely devoid of density at the extracellular entrance—and uncovered the conformational plasticity of this site, which will be further discussed in the next section.

Our analysis showed that under ATP-free condition, ~39% of particles exhibited an empty pore, 9% showed a strong pore-blocking density, and the remainder displayed weak residual density (Supplementary Fig. 3b)—likely representing partially occupied endogenous metabolites and/or solvent—which could not be confidently further classified as either strong-blocking or empty, as was also the case in the other datasets. In contrast, upon ATP supplementation, the proportion of particles with an empty pore markedly decreased to 12–18%, accompanied by a corresponding increase in particles with strong pore-blocking density to 28–31% (Supplementary Fig. 3b). Importantly, this trend was consistently reproduced across three independently collected and processed datasets at 10, 20, and 30 mM ATP. The percentage of particles with strong pore-blocking density was comparable across these datasets, serving not only as a reflection of the saturating effect of ATP—consistent with functional data showing maximal inhibition near 1 mM—but also as independent, replicative assessments that underscore the robustness and reproducibility of our classification framework (Supplementary Fig. 3b). While a smaller fraction of strong-blocking particles was also present in the absence of added ATP—likely reflecting residual endogenous metabolites engaging PANX1—the ATP-dependent increase in occupancy supports the interpretation that the pore-blocking density likely represents ATP binding. Because no major structural differences were observed among cryo-EM maps with strong pore-blocking density and those without across the four datasets—as expected, we combined the particles with strong pore-blocking density from the three ATP-supplemented datasets and the particles without such density from all datasets to increase particle numbers and improve map resolution (Supplementary Fig. 4). Both combined sets were refined to yield the final reconstructions: putative ATP-bound (combined) and apo (combined) (Supplementary Fig. 3b).

The putative ATP density is more pronounced than the signal observed for most parts of the protein (Fig. 1b, c), consistent with ATP's inherently stronger electron density due to its phosphorus atoms, which scatter electrons more effectively than the lighter atoms in amino acid residues, thereby providing evidence consistent with ATP binding²⁷. The inverted cone-shaped density was compatible with that of an ATP molecule. Nonetheless, the exact ATP pose could not be resolved unambiguously, likely due to rotational and translational flexibility along the symmetric pore axis, resulting in a blurred, spindle-

shaped density. Accordingly, while the precise chemical nature of this density cannot be established unambiguously, the evidence indicates it is most consistent with ATP. We hypothesize that this density may represent ATP either transiently trapped during permeation or acting as a pore blocker—two functionally distinct but structurally indistinguishable states. Notably, the ATP-free structure represents a bona fide apo state of PANX1 without any density blocking the entry (Fig. 1c), which, to our knowledge, has not been captured in any of the previously reported PANX1 structures. In those structures, residual signal was always present at the extracellular entrance, likely due to co-purified endogenous ligands.

To validate this assignment, we replaced the key interacting residue W74 with alanine and determined its structure with 10 mM ATP (Supplementary Fig. 5). This structure is nearly identical to that of the wild type, with a backbone root-mean-square deviation (RMSD) of 0.3 Å, except for the absence of both the W74A sidechain and the pore-blocking density at the extracellular restriction site (Supplementary Fig. 3a). This supports the role of W74 in accommodating the hydrophobic adenine moiety of ATP. Additionally, the triphosphate group could establish favorable electrostatic interactions with R75 (Supplementary Fig. 3c), implicating positive charges at the extracellular entrance as critical for ATP binding and permeation. This interpretation is consistent with reduced ATP inhibition observed in the R75A/C/E mutants but not in the conservative R75K mutant²⁸.

W74 plasticity adjusts extracellular pore entrance

The putative ATP density near W74 in the extracellular restriction site provides structural basis for understanding ATP permeation and inhibition, while also establishing this site as a central gating and selectivity element in PANX1. Interestingly, the W74 density in the consensus cryo-EM map appears to adopt at least two distinct conformations (marked by two arrows in Supplementary Fig. 6a), suggesting inherent structural heterogeneity. To explore whether and how this structural variability contributes to permeation and gating, we next focused on the plasticity of the extracellular entrance. To improve classification, we pooled all datasets (0, 10, 20, and 30 mM ATP), which increased particle numbers and yielded an improved overall resolution of 2.5 Å (Supplementary Fig. 2). This approach was feasible because the datasets differ only in the fraction of particles displaying putative ATP density at the pore entrance; combining them enhanced the chances of resolving distinct conformations without introducing additional structural heterogeneity. We then performed focused classification on particles that lacked strong pore-blocking density, as the prominent density, when present, could bias the classification by dominating adjacent structural features. This strategy revealed a spectrum of conformational states at the extracellular entrance (Supplementary Fig. 6b). These changes appear to span a continuum, with each state characterized by a distinct pose of the W74 sidechain and its interaction with R75, resulting in variable cation–π interaction geometries and pore architectures. These conformations likely modulate cargo permeation by altering the size of the extracellular entrance.

For the ease of discussion, we focus on two extreme conformational states captured in our merged dataset, corresponding to the smallest and largest pore openings: constricted (merged) and dilated (merged). These states show distinct W74 sidechain orientation, resulting in a constricted or dilated extracellular pore entrance (Fig. 2a,b; Supplementary Table 2). In the constricted conformation, the long axis of the W74 indole ring lies roughly parallel to the membrane plane, with adjacent W74 residues arranged at ~50° angles (Fig. 2c). This configuration forms a constricted ring of seven indole side chains. Notably, in this conformation, the W74 side chains are relatively distant (~6 Å) from the guanidinium group of R75, suggesting minimal cation–π interaction (Fig. 2c). Thus, the stability of this state appears to be driven primarily by W74–W74 interactions.

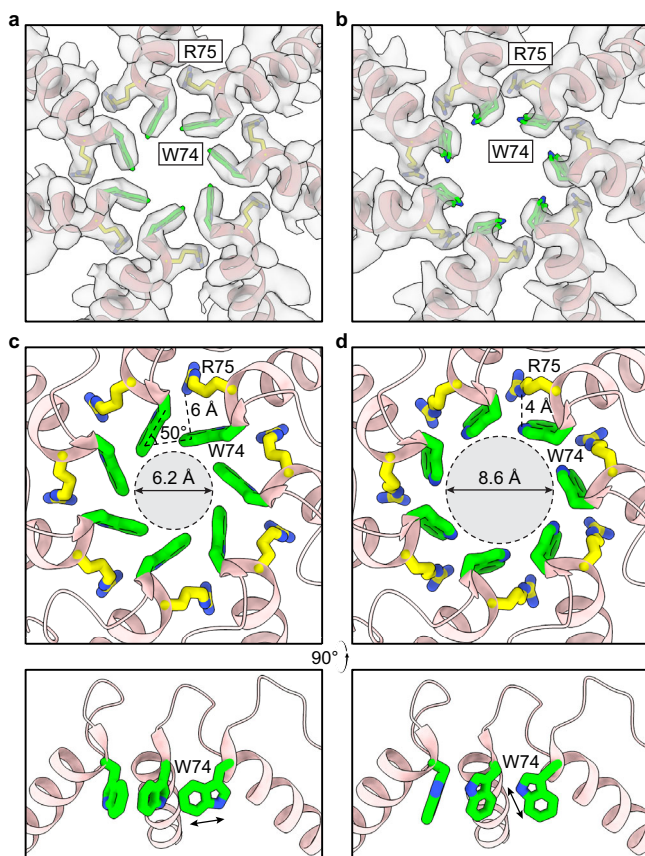


Fig. 2 | Plasticity of the extracellular restriction site. **a, b** Constricted (a) and dilated (b) conformations of the extracellular restriction site, obtained through ECD-focused classification of the merged dataset (see Results, “W74 plasticity adjusts extracellular pore entrance”). Structures are viewed from the extracellular side. Cryo-EM maps are shown as transparent envelopes. PANX1 atomic models are displayed in cartoon representation, with the side chains of W74 and R75 shown as sticks. **c, d** Close-up views of the extracellular restriction site in the constricted (c) and dilated (d) conformations. The upper panels show extracellular views, with interactions between W74 and R75 indicated by dashed lines and their distances labeled. The angle between adjacent W74 side chains in the constricted conformation and the pore diameters in both conformations are indicated. The lower panels show views parallel to the membrane, with the long axes of the W74 side chains indicated by double-headed arrows.

In contrast, the dilated conformation involves a near 180° rotation of the W74 side chain around the C α -C β bond relative to the constricted conformation, orienting the indole ring perpendicular to the membrane plane (Fig. 2d). This reorientation increases the spacing between neighboring W74 residues while bringing the indole ring into closer proximity (~ 4 Å) to the R75 guanidinium group, consistent with a stronger cation-π interaction (Fig. 2d). Therefore, unlike the constricted conformation, the dilated conformation appears to be stabilized primarily by the cation-π interaction between W74 and R75.

Importantly, while the extracellular domain—including the backbone of the restriction site (W74 and R75)—remained unchanged, the side chain movement of W74 markedly adjusted the diameter of the extracellular entrance, from 6.2 Å to 8.6 Å (Fig. 2c,d). The pore size of the constricted state approximates that of a hydrated chloride ion, suggesting that this state represents a previously unrecognized ion-conducting conformation for only small anions. In contrast, although the dilated state remains narrower than a fully hydrated ATP molecule

(~ 12 Å)²⁴, our structures suggest that the extracellular entrance is sufficient to accommodate ATP, likely involving partial dehydration. The dehydrated ATP may form favorable interactions with W74 and R75, either during permeation as a cargo molecule or when acting as a pore blocker, thereby compensating for the energy cost of dehydration.

Consistent with this structural heterogeneity, our whole-cell patch-clamp measurements revealed that ATP-mediated inhibition is incomplete, with maximal inhibition reaching only ~75% even at saturating ATP concentrations (Fig. 1a). This partial inhibition suggests that PANX1 exists in at least two conformational states: one that is sensitive to ATP blockage and another that remains resistant—a distinction directly supported by our structural analysis.

Together, these findings support a model in which the extracellular entrance of PANX1 exhibits structural plasticity, enabling dynamic regulation of cargo permeation and binding of pore blockers through local conformational rearrangements (Supplementary Video 1), where the cation-π interaction between W74 and R75 plays a role in shaping the extracellular pore geometry. Our findings also align with previous functional studies showing that PANX1 can adopt distinct open states with different pore sizes, where a low-conductance conformation permits small anions, while a high-conductance conformation allows ATP permeation²⁹.

Mefloquine potentiates PANX1 activity

The antimalaria drug mefloquine has been reported to inhibit various large-pore channels, including PANX1, connexins, and volume-regulated anion channels^{30–32}. However, its impact on PANX1 remains controversial due to conflicting reports on its inhibitory effect^{33–36}. In light of these debates, we conducted electrophysiology experiments using mefloquine from two independent vendors, as the discrepancies in the literature have been attributed to different mefloquine sources/stereoisomers (Supplementary Fig. 7)³⁰. Our result showed that application of the Bioblocks (R*,S*)-mefloquine and the SelleckChem (R,S)-mefloquine, but not the Bioblocks (R*,R*)-mefloquine, markedly increased the human PANX1 currents that were sensitive to CBX inhibition (Fig. 3a; Supplementary Figs. 8a–h), although we are unable to explain the disparity between our experiment and previous studies that both involved the Bioblocks (R*,S*)-mefloquine. The potentiating effect was reversible, with the currents returning to baseline levels after washout of the compound (Supplementary Fig. 8i). Furthermore, the effect of mefloquine on PANX1 conductance was notably more pronounced at more positive potentials, indicating a potential synergistic interplay between mefloquine and membrane depolarization (Fig. 3b; Supplementary Fig. 8j). Given that the ionic conductance of full-length PANX1 upon membrane depolarization is primarily mediated through the side tunnel pathway¹³, our findings suggest a potential connection between mefloquine modulation and side tunnel gating.

Mefloquine binds near the side tunnel

Our electrophysiological studies have unveiled mefloquine as a positive modulator of PANX1. To identify its binding site on PANX1 and investigate the molecular mechanism of potentiation, we determined the structure of PANX1 in complex with mefloquine at a resolution of 2.7 Å (Supplementary Fig. 9; Supplementary Table 3). The high-quality map allowed us to observe a strong density within the crevice between the TMDs of adjacent subunits, proximal to the side tunnel (Fig. 3c). The shape of this density corresponds to that of a mefloquine molecule (Fig. 4a, left panel), in which the fluoromethyl-quinoline moiety engages hydrophobic residues from helices NTH, S1 and S2, while the piperidin group orients towards the side tunnel, making direct contact with the NTH-S1 linker. When superimposing a single subunit from the mefloquine-bound and apo PANX1 structures, the TMD of the neighboring subunit underwent a rotational movement, which in turn,

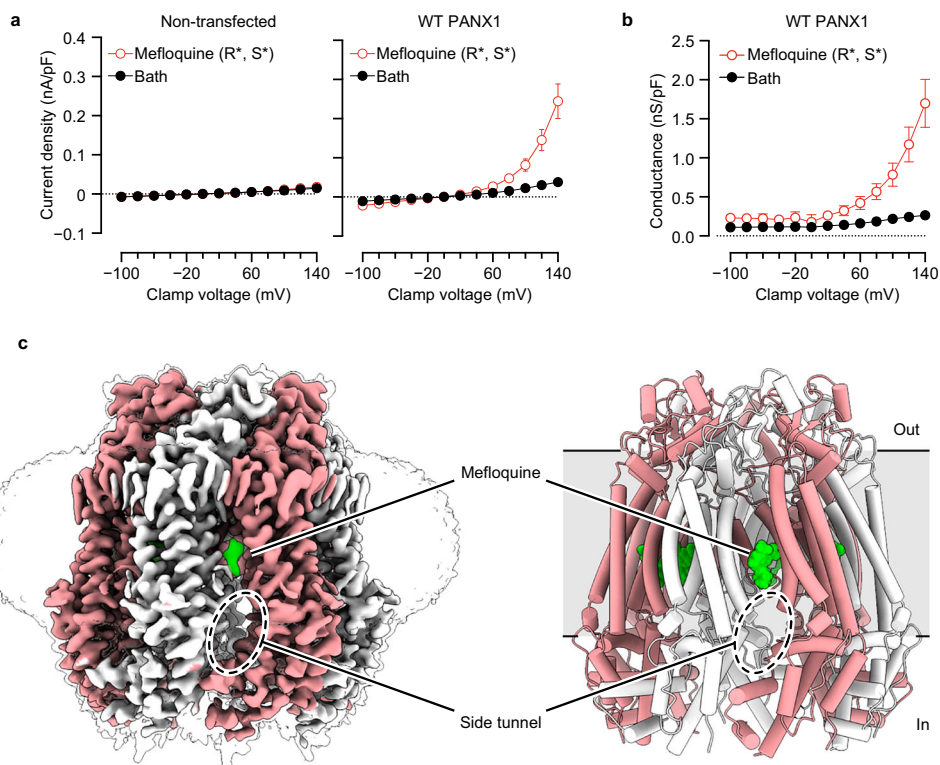


Fig. 3 | Mefloquine potentiates PANX1 channel activity. **a** Current-voltage relationships of non-transfected tsA201 cells (left, $n = 6$) and cells overexpressing wild-type (WT) PANX1 (right, $n = 7$) pre- and post-perfusion with 150 μ M mefloquine in the bath solution. Circles represent mean current, and error bars represent s.e.m. Here and below, n represents the number of independent cells recorded in whole-cell patch clamp experiments. **b** Voltage-conductance relationships of tsA201 cells

overexpressing wild-type PANX1 before and after perfusion with 150 μ M mefloquine in the bath solution ($n = 7$). Circles represent mean, and error bars represent s.e.m. **c** Cryo-EM maps (left) and atomic model (right) of PANX1 with mefloquine (EMD-70769 and 9OQP). The structures are viewed parallel to the membrane. The mefloquine density is colored in green. The location of the side tunnel is also indicated. The cryo-EM map is C7 refined and are contoured at 6 σ level.

altered the structural elements lining the side tunnel (Fig. 4b). Interestingly, despite obvious rearrangement of the intersubunit interface, mefloquine binding induced only subtle yet discernible conformational changes in the surrounding residues (Fig. 4a, left panel). This may be due to the fact that the cleft was occupied by a lipid density in the apo structure (Fig. 4a, right panel)¹³, which allows mefloquine, also with a lipophilic nature, to fit into it without causing major conformational shifts in the binding site.

Since the “mefloquine site” is the first regulatory site identified in pannexin channels that allosterically potentiates channel function, we validated the binding site through systematic site-directed mutagenesis and electrophysiological experiments (Fig. 4c; and Supplementary Fig. 10). To perturb mefloquine binding, we introduced mutations by replacing key interacting residues with alanine or phenylalanine. Additionally, we generated a truncation construct ($\Delta 2-20$) by removing the NTH which formed multiple interactions with the putative mefloquine density. Notably, five out of the nine mutants (I41A, L125A, I41F, L125F, and $\Delta 2-20$) displayed a loss of potentiation effect by mefloquine (Fig. 4c). Conversely, the V11F variant (but not the V11A), located on NTH, became hypersensitive to mefloquine potentiation (Fig. 4c). Moreover, the alanine and phenylalanine mutations of C40, situated on the S1 helix and representing the only polar residue constituting the mefloquine binding site, showed contrasting phenotypes –while C40A was inhibited by mefloquine, C40F became hypersensitive to mefloquine potentiation (Fig. 4c). Collectively, our electrophysiological data support the density bound within the intersubunit interface of the TMD near the side tunnel represents mefloquine.

Interestingly, we found that even subtle alterations within the mefloquine binding site exerted a remarkable influence on PANX1 activity, with single-residue substitutions, such as L125A/F, C40A, and

I41A/F) resulting in an 8- to 18-fold increase in basal channel activity that was sensitive to CBX inhibition (Fig. 4c; and Supplementary Figs. 10,11). Although the precise mechanisms of these phenotypes remain elusive, these observations indicate that changes near the side tunnel may influence channel activity. Supporting this notion, tunnel blocking mutant (A33W) and tunnel opening mutant (R29A) both became non-sensitive to mefloquine treatment (Fig. 4c; and Supplementary Fig. 10j,k)¹³. This insight highlights the “mefloquine site” as a previously unrecognized druggable target for developing compounds that allosterically modulate the functions of large-pore channels.

Mefloquine remodels side tunnel dynamics

We hypothesized that mefloquine potentiates PANX1 by modulating the conductance of the side tunnel, given the close proximity of the mefloquine binding site to the side tunnel and the remarkable effects of binding site mutants on ionic conductance through the side tunnel. Since the side tunnel is primarily governed by the NTH–S1 linker, a region of high flexibility, we combined molecular dynamics (MD) simulations and electrophysiology to investigate whether mefloquine affects the conformational dynamics of the side tunnel, thereby establishing the mechanism underlying mefloquine modulation.

We performed 600 ns unbiased MD simulations of PANX1 with and without mefloquine. Exploiting PANX1's heptameric structure with 7 side tunnels, our analysis of side tunnel dynamics extended the effective simulation time by 7-fold to 4.2 μ s, substantially enhancing the sampling efficiency. Tunnel analysis at the inter-subunit interface revealed two pathways, Tunnel 1, and Tunnel 2, separated by the NTH-S1 linker, that share an intracellular entry but diverge in their access to the main pore (Fig. 4d). These pathways displayed variable length and bottleneck radius throughout the simulation, influenced by

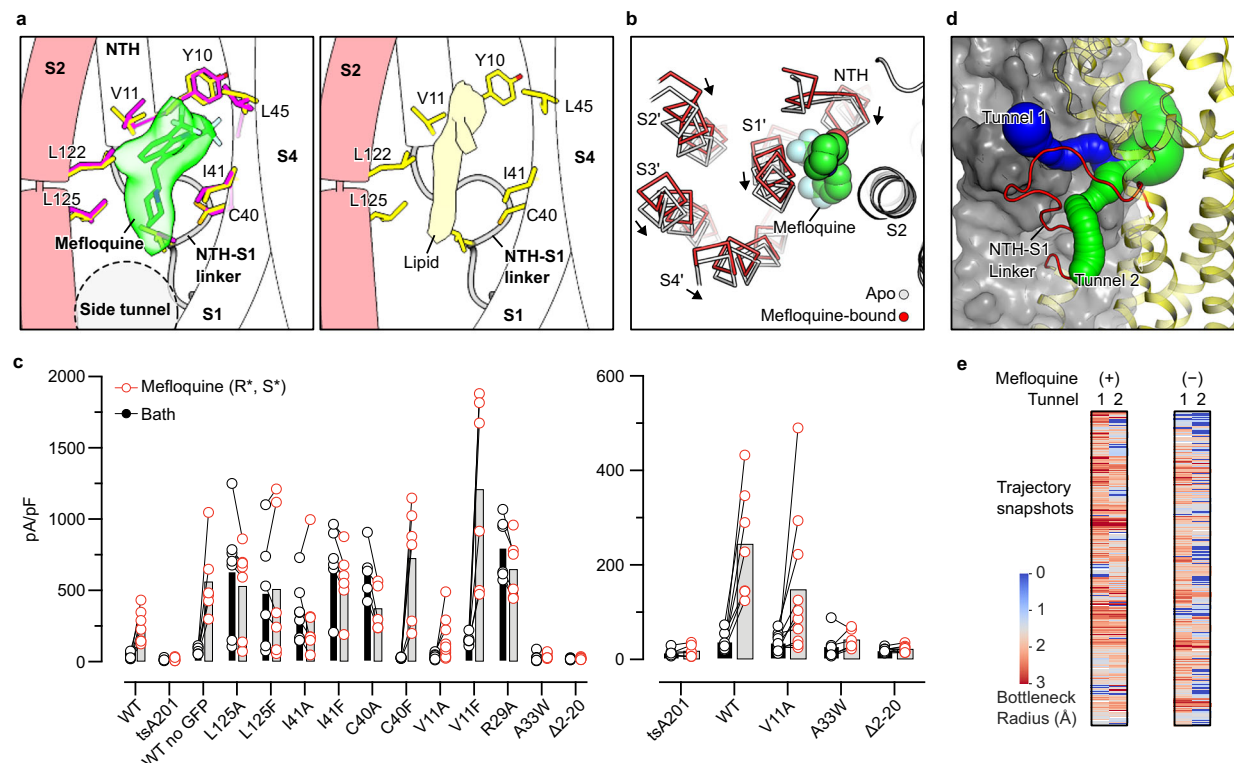


Fig. 4 | Mefloquine binding site and potentiation mechanism. **a** A close-up view of the mefloquine binding site, with mefloquine (green) and adjacent residues (magenta, PDBID: 9OQP) shown in stick representation. The corresponding residues in the apo state (yellow, PDBID: 6WBF) are superimposed. The cryo-EM density for mefloquine is shown in transparent green surface (EMD-70769). The lipid density observed in the apo state of PANX1 is shown as a yellow surface on the left (EMD-21589). **b** Superimposition of a single subunit (with residues 114–126, including binding site residues on this subunit) of the apo (yellow, PDBID: 6WBF) and mefloquine-bound (magenta, PDBID: 9OQP) PANX1 structures, showing the relative rotational movement of the neighboring subunit as indicated by the arrows. **c** Whole-cell currents at a holding potential of +140 mV from cells over-expressing wild-type PANX1 and mutants measured pre- and post-perfusion with

150 μ M mefloquine. Bars and circles represent mean current and individual cells. The number of cells measured: non-transfected tsA201, $n = 6$; hPANX1(WT) no GFP, $n = 6$; PANX1(WT), $n = 7$; V11A, $n = 10$; I41A, $n = 8$; L125A, $n = 7$; C40A, $n = 5$; V11F, $n = 6$; I41F, $n = 6$; L125F, $n = 6$; C40F, $n = 6$; R29A, $n = 6$; A33W, $n = 6$; $\Delta 2-20$, $n = 8$. The right panel shows a zoom-in view of V11A, A33W, and $\Delta 2-20$ with small current densities. **d** Two possible side tunnel pathways (Tunnel 1 and Tunnel 2) separated by the NTH-S1 linker, located at the interface between two adjacent subunits. One subunit is shown in yellow cartoon, and the other subunit is shown in gray surface representation. **e** The bottleneck radius profiles of the T1 and T2 pathways during the MD simulations in the absence (right) and presence (left) of mefloquine. Snapshots are sampled every 1.5 ns.

the flexible NTH-S1 linker and the inter-subunit interface (Fig. 4d; and Supplementary Videos 2 and 3). Notably, mefloquine binding led to an expansion of the bottleneck in both pathways (Fig. 4e; and Supplementary Fig. 12a), supporting our hypothesis that mefloquine potentiates PANX1 channel activity by modulating the dynamics of the side tunnel.

To investigate how mefloquine remodels side tunnel dynamics, we assessed residue flexibility within the TMD by comparing the averaged root-mean-square-fluctuation (RMSF) in the absence and presence of mefloquine. Remarkably, while mefloquine binding decreased the overall TMD flexibility—an expected outcome due to its binding in the intersubunit interface, thereby stabilizing the TMD—the NTH-S1 linker showed an unexpected increase in flexibility (Supplementary Fig. 12b, c). This can be attributed to the direct contact of mefloquine with the first few residues of NTH-S1 linker, including D14, F15 and L16, causing alterations in their backbone torsion angles (ϕ , ψ). Consequently, these residues can sample additional regions in the Ramachandran space, thus adopting more conformations that were inaccessible in the absence of mefloquine (Supplementary Fig. 12d). Given that these residues constitute one of the two anchor points of the NTH-S1 linker, mefloquine-induced conformational changes may propagate to the NTH-S1 linker, and ultimately modulating the side tunnel conductance. This proposed mechanism aligns with our electrophysiological result demonstrating that mefloquine had limited

effect in modulating A33W and R29A, two variants previously shown to block or increase side tunnel conductance, respectively (Fig. 4c)¹³. Importantly, both the A33W and R29A mutations are unlikely to directly affect the mefloquine binding pocket, as the sidechain of A33/R29 is more than 10 \AA away from the mefloquine.

Discussion

Recent advances in high-resolution cryo-EM structure determination of large pore channels have revealed relatively constrained (<10 \AA in diameter) ion-conducting pores in pannexins and VRACs. This has prompted speculation about the compatibility of these available PANX1 and VRAC structures with the permeability of larger cargos like ATP, which has a hydrated radius of ~12 \AA ^{24,37}. It has been suggested that other conformational states of PANX1 and VRAC, particularly a substantially enlarged pore within the ECD, remain to be discovered^{24,37}. This raises a broader question: how do these channels transition between distinct transport modes—one that supports the permeation of small anions, and another that enables the regulated release of larger signaling molecules like ATP? These modes are not structurally or energetically equivalent, implying that large-pore channels must be tightly and dynamically regulated to switch between them according to physiological demand.

In this study, under ATP-supplemented conditions, we obtained clear cryo-EM maps showing either strong pore-blocking density, or

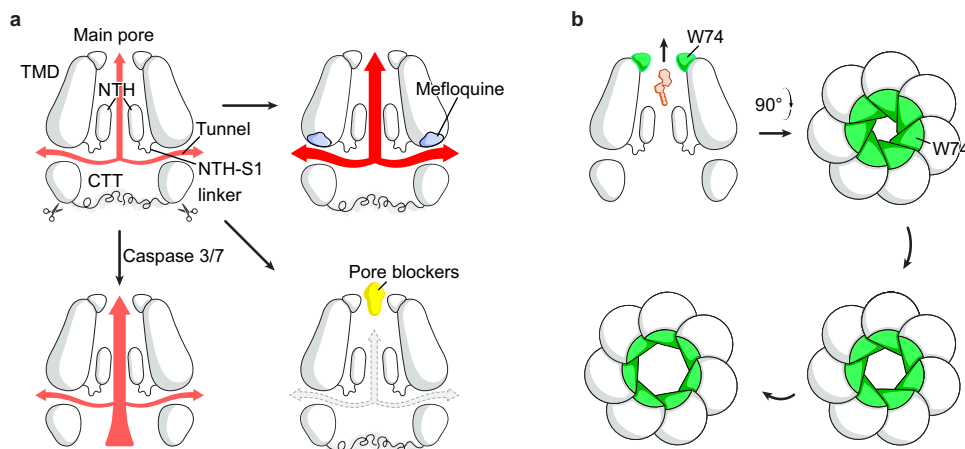


Fig. 5 | Proposed working model of PANX1. **a** Illustration of the permeation pathways of PANX1, highlighting allosteric modulation and channel blocking mechanisms. **b** Dynamics of the extracellular restriction site. Both the main pore and the side tunnel conduct ions like chloride. Removal of the C-terminal tail (CTT) via caspase 3/7 opens the cytoplasmic entrance of the main pore, enabling ATP

release. Disease-associated mutations in the NTH-S1 linker leads to increased ATP release¹¹, suggesting that the side tunnel may also allow ATP passage, a hypothesis that is supported by MD simulation studies but remains to be confirmed experimentally⁴³.

complete absence of such density at the extracellular entrance, representing putative ATP-bound and bona fide apo states of PANX1, respectively. If our interpretation of ATP binding is correct, the evidence would indicate that ATP occupies the extracellular restriction site of PANX1 without substantial expansion of the ECD. Instead, we hypothesize that ATP binding, and perhaps its permeation, is facilitated by the intrinsic sidechain plasticity of W74. Consistent with this hypothesis, we also resolved two distinct conformational states of the extracellular entrance, a constricted and a dilated state, defined by the orientation of the W74 sidechain. The constricted state, which narrows the pore to ~6 Å, is particularly striking and, to our knowledge, represents the first structural demonstration of an ion-conducting conformation for small anions within the pannexin family. In contrast, the dilated state expands the extracellular pore to accommodate partially dehydrated ATP. Together, these states offer a plausible mechanism for how PANX1 dynamically adjusts its pore size to accommodate diverse cargos. The dynamics of W74, therefore, play a central role in regulating cargo flux through the extracellular entrance (Fig. 5; and Supplementary Video 1). Given the hydrophobic nature of W74, dehydration likely precedes ATP binding. However, the favorable interaction between W74 and the hydrophobic adenine group of ATP may offset the unfavorable dehydration of ATP.

The dual roles of ATP as both substrate and blocker suggest a feedback mechanism that modulates the permeability of PANX1 and controls the cellular release of ATP, thereby influencing various physiological and pathological processes. It would be intriguing to explore whether VRAC, a related family with a heteromeric extracellular restriction site controlled by arginine (LRRC8A/B), leucine (LRRC8C/E), and phenylalanine (LRRC8D) residues^{38,39}, also employs sidechain dynamics to regulate pore size and cargo passage.

The PANX1 channel features two ion-conducting pathways, the main pore along the symmetry axis and seven side tunnels, which have different cytoplasmic entrance, but both converge at the common extracellular restriction site. Our studies of small-molecule compounds on PANX1 revealed two distinct modulation sites that control ion conductance through the main pore and side tunnels, respectively. The first one is the extracellular restriction site, common for PANX1 channel blockers including CBX and ATP. This is analogous to the pore-blocking mechanism found in VRAC with DCPB⁴⁰. However, due to its intrinsic biophysical properties—large diameter and homogeneous amino acid composition—the extracellular restriction site is unlikely to exhibit strict selectivity for small molecule compounds.

The second modulation site, referred to as the “mefloquine site” in this study, is located between adjacent subunits near the side tunnel. We identified mefloquine as a potentiator for PANX1 and elucidated the modulation mechanism by which mefloquine altered the dynamics of the NTH-S1 linker, a key gatekeeper of the side tunnel, leading to the expansion of the side tunnel for ionic conduction (Fig. 5; and Supplementary Video 4). Moreover, we showed that the mefloquine binding site is sensitive to alterations, as mutations profoundly impacted the basal channel activation, likely achieved by altering the conductance of the side tunnels. While our structural data suggest that the side tunnels primarily accommodate small ions, such as chloride, recent results from steered molecular dynamics simulations have demonstrated that these tunnels might also allow the passage of ATP⁴¹. Supporting this notion, mutations in the NTH-S1 linker, which gates these tunnels, lead to human oocyte death by increasing the PANX1-mediated ATP release¹². Therefore, the mefloquine site holds immense potential for rational design of small-molecule compounds to control channel activity and treat PANX1 channelopathy. In addition, a recent metabolomics screening study identified lysophospholipids (LPC) as a potential positive regulator of PANX1⁴². While structural evidence of the LPC binding site is still lacking, molecular docking analysis showed that LPC occupies a location similar to the “mefloquine site”, implying that endogenous lipids might exploit this site as well⁴². This is consistent with our structural data revealing a putative lipid density at the “mefloquine site” in the apo structure of PANX1¹³. More importantly, the conserved TMD organization among large-pore channel families suggests that the “mefloquine site” is, in principle, present across all large-pore channels^{7,13}. For example, in the recently resolved high-resolution structures of PANX2, PANX3 as well as the related connexin 50 and LRRC8A, the “mefloquine site” is occupied by lipid densities (Supplementary Fig. 13a), resembling the “mefloquine site” in the apo state structure of PANX1 (Fig. 2b)^{43–45}. Given the reported mefloquine sensitivity of connexin and VRAC channels^{31,32}, we speculate that mefloquine may also modulate these channels through similar sites.

In contrast to the relatively homogeneous composition of the extracellular restriction site, which makes it unlikely to be selective for drug binding, the distinct amino acid compositions of the “mefloquine site” in various large-pore channels offer a unique advantage (Supplementary Fig. 13b), potentially enabling the development of long-sought specific modulators capable of discerning between different large-pore channel types. The discovery of the “mefloquine site” thus opens avenues for innovative drug development targeting both PANX1

and other related large-pore channels. This prospect is further reinforced by recent studies published during the review of this article, which revealed that mefloquine binds to connexin 32 and connexin 36 channel at similar sites as reported in our study^{46–48}.

Methods

DNA constructs and Reagents

Full-length human *PANX1* gene in pEG BacMam vector from our previous study is used for protein expression¹³. Specifically, the expression cassette contains the *PANX1* gene followed by a thrombin cleavage site, an enhanced green fluorescence protein (eGFP), and an 8xHis tag. The PCR primers for site-directed mutagenesis were designed using QuikChange Primer Design (<https://www.agilent.com/store/primerDesignProgram.jsp>) or NEBaseChanger (<https://nebasechanger.neb.com/>) webserver. The QuikChange or Q5 site-directed mutagenesis protocol from the manufacturer was used to introduce point mutations. The primer sequences used in this study are provided (Supplementary Table 4). All mutated constructs were confirmed by Sanger sequencing from Eurofins Genomics.

The adenosine 5'-triphosphate disodium salt hydrate (ATP) (Catalog A2383) is obtained from Sigma-Aldrich. The mefloquine hydrochloride is obtained from BioBlocks (Catalog QU024-1 and QU025-1) and SelleckChem (Catalog S4420). The Gibco Sf9 cells (Catalog 12-659-017) are obtained from Fisher Scientific. The tsA201 cells (Catalog CRL-3216) are obtained from ATCC.

Human PANX1 protein expression and purification

To produce baculovirus, pEG Bacman vector with human PANX1 with a GFP tag at the C-terminus is transformed into DH10Bac cells for bacmid generation. Purified bacmid was transfected into Sf9 cells in adherent culture using CellFectin II reagent (Gibco). After 5 days, the media containing P1 virus was harvested and used to infect Sf9 cells in suspension culture at a ratio of 1:5000 (v/v). P2 viruses (8%) were harvested after 4 days and used to infect tsA201 cells grown in suspension culture at 3–4 × 10⁶ cells/mL density. The cells were maintained at 37 °C for 8–16 h. Subsequently, 5 mM sodium butyrate was added to the culture to boost protein expression. The culture was then maintained at 30 °C in a shaking incubator. At about 60 h post-infection, the cells were harvested by centrifugation at 2880 × g, 4 °C for 15 min. Cell pellets were washed with TBS buffer (150 mM NaCl and 20 mM Tris pH 8.0) and stored at –80 °C.

For structural studies of human PANX1 with ATP, 1 L cell pellets expressing PANX1 were thawed on ice and resuspended in TBS buffer supplemented with protease inhibitors (1 mM PMSF, 0.8 μM aprotinin, 2 μg/mL leupeptin, and 2 mM pepstatin A). Cells were lysed by sonication and cell debris was removed by centrifugation at 3234 × g for 10 min. Membranes were isolated by ultracentrifugation at 200,000 × g for 1 h, washed twice with pre-chilled TBS buffer, and homogenized using a Dounce homogenizer. Then a 30 mL membrane fraction was dialyzed in 5 L of TBS buffer under continuous stirring, with dialysis buffer exchanged twice a day. After 7 days, membranes were solubilized in 1% glyco-diosgenin (GDN) supplemented with protease inhibitors for 1.5 h with gentle agitation. The solubilized material was clarified by centrifugation at 3234 × g for 10 min and ultracentrifugation at 200,000 × g for 1 h. The supernatant was incubated with 6.5 mL TALON resin (Takara Bio) pre-equilibrated with TBS buffer containing 0.01% GDN. Imidazole (10 mM) was added to reduce non-specific binding. After 1 h of batch binding, the resin was washed with twenty column volumes of TBS buffer containing 0.01% GDN and 20 mM imidazole. PANX1 was eluted with TBS buffer containing 0.01% GDN and 250 mM imidazole. The eluent was concentrated to 500 μL using a 100 kDa cutoff concentrator (Millipore). The C-terminal GFP tag was cleaved by overnight incubation with thrombin, using a protein-to-enzyme mass ratio of 200:1. GFP-cleaved protein was

further purified by size-exclusion chromatography on a Superose 6 Increase 10/300 GL column (GE Healthcare) in TBS buffer containing 0.01% GDN. Peak fractions were pooled and concentrated to 5 mg/mL for cryo-EM grid preparation. All the membrane preparation, dialysis and purification were performed at 4 °C. For structural studies of human PANX1 in the presence of mefloquine or the W74A mutant with 10 mM ATP, protein was extracted by whole cell solubilization using 1% GDN and purified following similar procedure described above, but without the membrane fraction dialysis.

Electron microscopy sample preparation and data acquisition

Freshly purified wild-type human PANX1 or the W74A mutant in GDN detergent was incubated with ATP or mefloquine at specified final concentrations prior to grid preparation. For ATP-containing grids, the final ATP concentrations were 0, 10, 20, or 30 mM. For mefloquine-containing grids, the final concentration of (R*,S*)-mefloquine (Bio-blocks; CAS# 51773-92-3 and 51688-68-7) was 1 mM. A 2.5-μL aliquot of the sample was applied to a glow-discharged Quantifoil holey carbon Au grid (2/1-μm size/hole space, 300-mesh), blotted for 2 s at 100% humidity in a Vitrobot Mark III chamber, and then plunge-frozen in liquid ethane cooled by liquid nitrogen. The grids were initially screened using an FEI Titan Talos Arctica transmission electron microscope operating at 200 kV with a Gatan K2 Summit direct electron detector.

For human PANX1 with 0/10/20/30 mM ATP dataset, high-resolution data was collected using a Glacios transmission electron microscope (Thermo Fisher Scientific) operating at 200 kV, equipped with a 10 eV slit-width energy filter and operated at a nominal magnification of ×130,000. Images were recorded using a Falcon 4i direct electron detector, yielding a physical pixel size of 0.91 Å. Each movie stack was acquired with a total electron dose of 40 e[–]/Å². Automated data acquisition was carried out using EPU 3.9.1 software, with a nominal defocus range of –0.6 to –1.2 μm or –1.3 to –1.8 μm.

For human PANX1 with 1 mM mefloquine and PANX1 W74A with 10 mM ATP datasets, high-resolution data collection was performed on a Titan Krios transmission electron microscope (Thermo Fisher Scientific) operating at 300 kV, equipped with a 20 eV slit-width energy filter and operated at a nominal magnification of ×130,000. Images were recorded using a K3 direct electron detector in super-resolution mode, yielding a physical pixel size of 0.406 Å (binned to 0.812 Å for data processing). Each movie stack was acquired with a total electron dose of 49.6 e[–]/Å². Automated data acquisition was carried out using SerialEM 4.15 software⁴⁹, with a nominal defocus range of –1.2 to –1.9 μm.

Cryo-EM data analysis procedure

The data processing workflow are summarized in Supplementary Figs. 1, 9a and Supplementary Fig. 5a. The final map statistics, local resolution overview and angular distribution can be found in Supplementary Tables 1–3, Supplementary Fig. 9c–d, and Supplementary Fig. 5c. Specifically, raw Videos were first motion-corrected using motioncor2 1.6.4 or relion 5.0^{50,51}. The contrast transfer function (CTF) of each micrograph was estimated using ctffind v.4.1.10 or v.4.1.14⁵². We used relion 5.0 or gautomatch 0.56 (<https://github.com/JackZhang-Lab/Gautomatch>) for template-based particle picking and topaz v0.2.5 for convolutional neural network-based particle picking⁵³. Low quality particles were removed by reference-free 2D classifications and heterogeneous refinement using relion 5.0 or cryosparc 4.6.0^{51,54}. Particle sets from different auto-picking runs were merged after cleanup. Duplicated particles were removed using a distance cutoff of 30 Å. The consensus map was generated by refining the merged particle set by imposing either C7 symmetry. Subsequently, the reconstruction was improved by supplying a soft solvent mask, followed by iterative CTF refinement and Bayesian polishing steps⁵⁵.

Classification strategy to resolve ATP-bound and ATP-free apo states at the extracellular restriction site

To distinguish ATP-bound and ATP-free (apo) states, we performed focused classification without image alignment after subtracting the extracellular domain (ECD). This classification is inherently challenging because small molecules of different sizes—such as endogenous metabolites, solvent, or detergent—may also bind to the extracellular restriction site and produce cryo-EM density, thereby complicating interpretation. Indeed, the classification yielded a continuum of classes with varying degrees of pore-blocking density, making it difficult to define clear ATP-bound and apo states. In addition, we note that the putative ATP-binding site lies along the C7 symmetry axis, where densities are prone to symmetry-related artifacts. To address this, we generated dataset of very comparable quantity and quantity and processed them using identical workflows, reasoning that any symmetry-related artifact (if present) would impact all datasets similarly (however, refinement without imposing symmetry revealed no obvious evidence of such artifacts; see Supplementary Fig. 4).

To address this, we established a stringent selection criterion based on the distinct signal characteristics of ATP in cryo-EM maps. Because ATP has a higher local electron density than surrounding amino acids, a true ATP-bound class is expected to exhibit strong, well-defined density at the restriction site. In contrast, a bona fide apo class should display a complete absence of density at this site. Accordingly, we selected only those classes with very strong pore-blocking density as putative ATP-bound, and those with no detectable density as apo.

Despite this effort, two complications remained. First, the structural difference between putative ATP-bound and apo states is small, leading to imperfect classification in which not all ATP-bound particles are grouped into the putative ATP-bound class, and some ATP-free particles are misclassified into the putative ATP-bound class. The same issue applies to the apo class.

To mitigate these challenges, we developed a reproducibility-driven classification framework. We repeatedly ran the focused classification and selected putative ATP-bound and apo classes using the criteria described above. From each classification run, particles assigned to the putative ATP-bound class were pooled, and duplicates were removed; the same procedure was applied to the apo class. This iterative approach assumes that ATP-bound and apo particles, if present, will have the opportunity to be correctly classified over multiple runs. By aggregating particles across repeated classifications, this strategy helps ensure that as many true ATP-bound and apo particles as possible are recovered, thereby improving the completeness of each class.

Following this pooling step, we applied a filtering procedure to eliminate particles that may have been misclassified into both sets. By comparing the two pooled groups, we retained only particles unique to each, ensuring that the final putative ATP-bound and apo classes were as distinct as possible.

To monitor convergence, we tracked the number of unique particles across classification jobs and proceeded to the next stage of processing only when these numbers stabilized. Once convergence was achieved, we reverted to the original, non-subtracted particle images and performed 3D refinement of both the putative ATP-bound and apo states. This entire classification framework was applied independently to each of the four datasets (0, 10, 20, and 30 mM ATP).

This approach proved effective for several reasons. First, the putative ATP-bound reconstructions consistently showed very strong pore-blocking density, consistent with the chemical nature of ATP, while the apo structures exhibited clean, unoccupied restriction sites—indicating reasonably successful separation of the two states. Second, comparison across datasets revealed a clear increase in putative ATP-bound particles and a corresponding decrease in apo particles upon ATP addition, strongly supporting that ATP binds to the extracellular restriction site. Third, the proportion of putative ATP-bound particles

was comparable across the 10, 20, and 30 mM ATP datasets, which were collected and processed independently. This is consistent with electrophysiological data showing that all three concentrations exceed the saturation point for ATP inhibition and would therefore be expected to exhibit similar ATP occupancy. Together, these results support the robustness and reproducibility of our classification strategy.

Finally, because we expected—and indeed observed—no structural differences among putative ATP-bound or apo states across the four datasets, we combined the putative ATP-bound particles from the three ATP-supplemented datasets and apo particles from all four datasets to increase particle numbers and improve map resolution. Both combined sets were refined to yield the final reconstructions.

Model building

The atomic models were generated by fitting PDB 6WBG into the final cryo-EM map¹³. Small molecules were fitting into the density through real-space refinement via coot 0.9.8.9⁵⁶. The cif library of small molecule was generated from Grade Web Server (https://grade.globalphasing.org/cgi-bin/grade2_server.cgi) using their SMILLE string. In particular, we used (R,S)-mefloquine (CAS# 51773-92-3) stereoisomer in the PDB 8UWK, PANX1(1 mM mefloquine). The models were then manually adjusted to ensure the fitting of residue sidechain and subjected to phenix real space refinement to improve the model metrics⁵⁷. The final models were validated using phenix.molprobity. Surface electrostatic potential was calculated using the ChimeraX 1.8 using the gasteiger method⁵⁸. Tunnel and pore size analysis were done using Caver 3.0 and Hole 2.0^{59,60}. Figures were generated using PyMOL 3.0.4 (Schrödinger LLC) and UCSF ChimeraX 1.8⁵⁹.

Molecular dynamics (MD) simulation

The MD system of pure 1-palmitoyl-2-oleoyl-sn-glycero-3-phosphocholine (POPC) lipid bilayer with PANX1 was constructed using CHARMM-GUI webserver⁶¹. Specifically, the PANX1 model was oriented with respect to the membrane normal utilizing the OPM server^{62,63}. Titratable residues of PANX1 protein were protonated based on neutral environment pH, and the system was solvated with TIP3P water molecules. To ensure overall charge neutrality, the system was neutralized with ~150 mM NaCl. More detailed simulation system information can be found in Supplementary Table 5. The CHARMM36m force field were employed to parameterize the MD system⁶⁴. Parameters for mefloquine was generated using the ligand preparation function of CHARMM-GUI⁶⁵.

Energy minimization step was performed using the steepest-descent algorithm with a Fmax tolerance of 1000 kJ mol⁻¹ nm⁻¹. Position restraints were applied to non-hydrogen atoms of the protein and the phosphorus atom of POPC. The system then underwent 6 rounds of equilibration, gradually reducing the strength of the position restraints. During the equilibration, the temperature of the system was increased to 310 K using a Berendsen thermostat in the NVT ensemble. Subsequently, the NPT ensemble was employed using a Berendsen semiisotropic pressure coupling at 1 bar. Hydrogen atom constraints were applied using the LINCS algorithm⁶⁶. The production simulation, without restraints, was conducted in the NPT ensemble using the Nose-Hoover thermostat and Parrinello-Rahman barostat. Three independent production simulations were conducted, each for 200 ns with a timestep of 2 fs. The Verlet cut-off scheme was utilized for the neighbor list (12 Å) to account for short-range electrostatic and van der Waals interactions. The Gromacs v.2019.2 software was employed as the molecular dynamics engine⁶⁷. Analysis of the trajectory data was performed using Gromacs utilities. The trajectories were confirmed to have reached equilibrium by monitoring the root mean square deviation (RMSD) of protein C_α atoms (Supplementary Fig. 14). Tunnel identification over the MD snapshots were analyzed by Caver 3.0⁵⁹. Tunnels in the structure were visualized using PyMOL 3.0.4⁵⁹.

Electrophysiology

Using patch-clamp analysis whole-cell currents were measured in tsA201 cells following 1–2 days of transient over-expression with Lipofectamine 2000. C-terminal GFP tagged human PANX1 constructs were used for visual identification. Untagged human PANX1 measurements relied on co-expression of a plasmid encoding GFP for identification. Patch pipettes contained a pH 7.3 solution composed of (in mM) 145 NaCl, 10 Hepes, 10 EGTA and the external bath was a pH 7.4 solution of 160 NaCl, 10 Hepes, 3 KCl, 2 CaCl₂, and 1 MgCl₂. Voltage steps of 0.25 s were imposed from −100 mV to +140 mV and membrane currents were recorded (digitized at 10 kHz and filtered at 2 kHz) using a Multiclamp 700B 2.2.2.2 (Axon Instruments) and Clampex software (11.3). Currents were first measured in the control bath solution and then after perfusion with bath solution containing either ATP at the indicated concentrations or 150 µM mefloquine (BioBlocks, Sell-eckchem). Current amplitudes were measured at 5 ms of the indicated clamp voltages and normalized to cell capacitance. Expression level of PANX1 mutants (V11A, A33W, and Δ2–20) with small current are found to be comparable to wild type PANX1 (Supplementary Fig. 15). All subsequent analyses and figure generation were performed in Python 3.11 using the following packages and versions: pyabf 2.3.7, NumPy 1.26.4, SciPy 1.11.4, and Matplotlib 3.8.4. Graphical visualizations of the processed data were performed using GraphPad Prism version 10.6.1 (GraphPad Software). All custom Python scripts used for ABF data processing, filtering, and visualization are available at <https://github.com/junuk861/panx1-ephys-analysis>.

Reporting summary

Further information on research design is available in the Nature Portfolio Reporting Summary linked to this article.

Data availability

The cryo-EM maps have been deposited in the Electron Microscopy Data Bank (EMDB) under accession codes [EMD-70760](#) (PANX1 (0 mM ATP) consensus); [EMD-70761](#) (PANX1 (10 mM ATP) consensus); [EMD-70762](#) (PANX1 (20 mM ATP) consensus); [EMD-70763](#) (PANX1 (30 mM ATP) consensus); [EMD-70764](#) (PANX1 (merged 0, 10, 20, 30 mM ATP datasets) consensus); [EMD-70765](#) (PANX1 (putative ATP-bound)); [EMD-70766](#) (PANX1 (Apo)); [EMD-70767](#) (PANX1 (Constricted pore)); [EMD-70768](#) (PANX1 (Dilated pore)); [EMD-70769](#) (PANX1 (1 mM mefloquine)); and [EMD-70770](#) (PANX1-W74A (10 mM ATP)). The atomic coordinates have been deposited in the Protein Data Bank (PDB) under accession codes [9OQG](#) (PANX1 (0 mM ATP) consensus); [9OQH](#) (PANX1 (10 mM ATP) consensus); [9OQI](#) (PANX1 (20 mM ATP) consensus); [9OQJ](#) (PANX1 (30 mM ATP) consensus); [9OQK](#) (PANX1 (merged 0, 10, 20, 30 mM ATP datasets) consensus); [9OQL](#) (PANX1 (putative ATP-bound)); [9OQM](#) (PANX1 (Apo)); [9OQN](#) (PANX1 (Constricted pore)); [9OQO](#) (PANX1 (Dilated pore)); [9OQP](#) (PANX1 (1 mM mefloquine)); and [9OQQ](#) (PANX1-W74A (10 mM ATP)). Previously published PDB codes used in this study: [6WBF](#) (PANX1); [6WBG](#) (PANX1-ΔCTT). Previously published EMDB codes used in this study: [EMD-21589](#) (PANX1-ΔCTT); [EMD-22358](#) (Connexin 50); [EMD-33276](#) (PANX2); [EMD-33273](#) (PANX3); [EMD-33527](#) (LRRC8A). The source data underlying Figs. 1a, 3a,b, 4c and Supplementary Figs. 3b, 8a, 8e, 8h–j, 10, and 11 are provided as a Source Data file. Files relating to the MD simulations have been deposited in Zenodo [<https://doi.org/10.5281/zenodo.17436693>]. Source data are provided with this paper.

References

- Burnstock, G. et al. Purinergic Signalling: Therapeutic Developments. *Front Pharmacol* **8**, 661 (2017).
- Taruno, A. et al. CALHM1 ion channel mediates purinergic neuro-transmission of sweet, bitter and umami tastes. *Nature* **495**, 223–226 (2013).
- Adamson, S. E. & Leitinger, N. The role of pannexin1 in the induction and resolution of inflammation. *FEBS Lett.* **588**, 1416–1422 (2014).
- Dale, N., Butler, J., Dospinescu, V.-M. & Nijjar, S. Channel-mediated ATP release in the nervous system. *Neuropharmacology* **227**, 109435 (2023).
- Sáez, J. C., Cisterna, B. A., Vargas, A. & Cardozo, C. P. Regulation of pannexin and connexin channels and their functional role in skeletal muscles. *Cell. Mol. Life Sci.* **72**, 2929–2935 (2015).
- Zhang, Z. et al. Regulated ATP release from astrocytes through lysosome exocytosis. *Nat. Cell Biol.* **9**, 945–953 (2007).
- Syrjanen, J., Michalski, K., Kawate, T. & Furukawa, H. On the molecular nature of large-pore channels. *J. Mol. Biol.* **433**, 166994 (2021).
- Crespo Yanguas, S. et al. Pannexin1 as mediator of inflammation and cell death. *Biochim Biophys. Acta Mol. Cell Res* **1864**, 51–61 (2017).
- Makarenkova, H. P., Shah, S. B. & Shestopalov, V. I. The two faces of pannexins: new roles in inflammation and repair. *J. Inflamm. Res* **11**, 273–288 (2018).
- Li, L., He, L., Wu, D., Chen, L. & Jiang, Z. Pannexin-1 channels and their emerging functions in cardiovascular diseases. *Acta Biochim Biophys. Sin. (Shanghai)* **47**, 391–396 (2015).
- Yeung, A. K., Patil, C. S. & Jackson, M. F. Pannexin-1 in the CNS: emerging concepts in health and disease. *J. Neurochem* **154**, 468–485 (2020).
- Sang, Q. et al. A pannexin 1 channelopathy causes human oocyte death. *Sci Transl Med* **11**, eaav8731 (2019).
- Ruan, Z., Orozco, I. J. & Du, J. & Lü, W. Structures of human pannexin 1 reveal ion pathways and mechanism of gating. *Nature* **584**, 646–651 (2020).
- Michalski, K. et al. The Cryo-EM structure of pannexin 1 reveals unique motifs for ion selection and inhibition. *Elife* **9**, e54670 (2020).
- Deng, Z. et al. Cryo-EM structures of the ATP release channel pannexin 1. *Nat. Struct. Mol. Biol.* **27**, 373–381 (2020).
- Mou, L. et al. Structural basis for gating mechanism of Pannexin 1 channel. *Cell Res* **30**, 452–454 (2020).
- Qu, R. et al. Cryo-EM structure of human heptameric Pannexin 1 channel. *Cell Res* **30**, 446–448 (2020).
- Jin, Q. et al. Cryo-EM structures of human pannexin 1 channel. *Cell Res* **30**, 449–451 (2020).
- Kuzuya, M. et al. Structures of human pannexin-1 in nanodiscs reveal gating mediated by dynamic movement of the N terminus and phospholipids. *Sci. Signal* **15**, eabg6941 (2022).
- Zhang, S. et al. Structure of the full-length human Pannexin1 channel and insights into its role in pyroptosis. *Cell Discov.* **7**, 30 (2021).
- Chekeni, F. B. et al. Pannexin 1 channels mediate ‘find-me’ signal release and membrane permeability during apoptosis. *Nature* **467**, 863–867 (2010).
- Dahl, G. et al. ATP release through pannexin channels. *Philos. Trans. R. Soc. Lond. B. Biol. Sci.* **370**, 20140191 (2015).
- Sabirov, R. Z. & Okada, Y. Wide nanoscopic pore of maxi-anion channel suits its function as an ATP-conductive pathway. *Biophys. J.* **87**, 1672–1685 (2004).
- Mim, C., Perkins, G. & Dahl, G. Structure versus function: are new conformations of pannexin 1 yet to be resolved? *J. Gen. Physiol.* **153**, e202012754 (2021).
- Jackson, D. G., Wang, J., Keane, R. W., Scemes, E. & Dahl, G. ATP and potassium ions: a deadly combination for astrocytes. *Sci. Rep.* **4**, 4576 (2014).
- Mansoor, S. E. et al. X-ray structures define human P2X3 receptor gating cycle and antagonist action. *Nature* **538**, 66–71 (2016).
- HALL, C. E. Electron densitometry of stained virus particles. *J. Biophys. Biochem Cytol.* **1**, 1–12 (1955).

28. Qiu, F. & Dahl, G. A permeant regulating its permeation pore: inhibition of pannexin 1 channels by ATP. *Am. J. Physiol. Cell Physiol.* **296**, C250–C255 (2009).

29. Wang, J. et al. The membrane protein Pannexin1 forms two open-channel conformations depending on the mode of activation. *Sci. Signal.* **7**, ra69–ra69 (2014).

30. Iglesias, R., Spray, D. C. & Scemes, E. Mefloquine blockade of Pannexin1 currents: resolution of a conflict. *Cell Commun. Adhes.* **16**, 131–137 (2009).

31. Cruikshank, S. J. et al. Potent block of Cx36 and Cx50 gap junction channels by mefloquine. *Proc. Natl. Acad. Sci. USA* **101**, 12364–12369 (2004).

32. Staines, H. M., Dee, B. C., Shen, M.-R. & Ellory, J. C. The effect of mefloquine and volume-regulated anion channel inhibitors on induced transport in Plasmodium falciparum-infected human red blood cells. *Blood Cells Mol. Dis.* **32**, 344–348 (2004).

33. Iglesias, R. et al. P2X7 receptor-Pannexin1 complex: pharmacology and signaling. *Am. J. Physiol. Cell Physiol.* **295**, C752–C760 (2008).

34. Suadicani, S. O., Brosnan, C. F. & Scemes, E. P2X7 receptors mediate ATP release and amplification of astrocytic intercellular Ca²⁺ signaling. *J. Neurosci.* **26**, 1378–1385 (2006).

35. Ma, W., Hui, H., Pelegrein, P. & Surprenant, A. Pharmacological characterization of pannexin-1 currents expressed in mammalian cells. *J. Pharm. Exp. Ther.* **328**, 409–418 (2009).

36. Silverman, W. R. et al. The pannexin 1 channel activates the inflammasome in neurons and astrocytes. *J. Biol. Chem.* **284**, 18143–18151 (2009).

37. Okada, Y., Sabirov, R. Z., Sato-Numata, K. & Numata, T. Cell death induction and protection by activation of ubiquitously expressed anion/cation channels. part 1: roles of VSOR/VRAC in cell volume regulation, release of double-edged signals and apoptotic/necrotic cell death. *Front Cell Dev. Biol.* **8**, 614040 (2020).

38. Kern, D. M. et al. Structural basis for assembly and lipid-mediated gating of LRRC8A:C volume-regulated anion channels. *Nat. Struct. Mol. Biol.* **30**, 841–852 (2023).

39. Syeda, R. et al. LRRC8 proteins form volume-regulated anion channels that sense ionic strength. *Cell* **164**, 499–511 (2016).

40. Kern, D. M., Oh, S., Hite, R. K. & Brohawn, S. G. Cryo-EM structures of the DCPIB-inhibited volume-regulated anion channel LRRC8A in lipid nanodiscs. *eLife* **8**, e42636 (2019).

41. López, X. et al. A physiologic rise in cytoplasmic calcium ion signal increases pannexin1 channel activity via a C-terminus phosphorylation by CaMKII. *Proc. Natl. Acad. Sci. USA* **118**, e2108967118 (2021).

42. Henze, E. et al. ATP-release pannexin channels are gated by lysophospholipids. *eLife* **14**, RP107067 (2025).

43. Flores, J. A. et al. Connexin-46/50 in a dynamic lipid environment resolved by CryoEM at 1.9 Å. *Nat. Commun.* **11**, 4331 (2020).

44. Zhang, H. et al. Cryo-EM structure of human heptameric pannexin 2 channel. *Nat. Commun.* **14**, 1118 (2023).

45. Liu, H. et al. Structural insights into anion selectivity and activation mechanism of LRRC8 volume-regulated anion channels. *Cell Rep.* **42**, 112926 (2023).

46. Cho, H.-J., Chung, D. K. & Lee, H. H. Mefloquine-induced conformational shift in Cx36 N-terminal helix leading to channel closure mediated by lipid bilayer. *Nat. Commun.* **15**, 9223 (2024).

47. Ding, X. et al. Structural basis of connexin-36 gap junction channel inhibition. *Cell Discov.* **10**, 68 (2024).

48. Lavriha, P. et al. Mechanism of connexin channel inhibition by mefloquine and 2-aminoethoxydiphenyl borate. *PLoS One* **19**, e0315510 (2025).

49. Mastronarde, D. N. Automated electron microscope tomography using robust prediction of specimen movements. *J. Struct. Biol.* **152**, 36–51 (2005).

50. Zheng, S. Q. et al. MotionCor2: anisotropic correction of beam-induced motion for improved cryo-electron microscopy. *Nat. Methods* **14**, 331–332 (2017).

51. Scheres, S. H. W. RELION: implementation of a Bayesian approach to cryo-EM structure determination. *J. Struct. Biol.* **180**, 519–530 (2012).

52. Rohou, A. & Grigorieff, N. CTFFIND4: fast and accurate defocus estimation from electron micrographs. *J. Struct. Biol.* **192**, 216–221 (2015).

53. Bepler, T. et al. Positive-unlabeled convolutional neural networks for particle picking in cryo-electron micrographs. *Nat. Methods* **16**, 1153–1160 (2019).

54. Punjani, A., Rubinstein, J. L., Fleet, D. J. & Brubaker, M. A. cryo-SPARC: algorithms for rapid unsupervised cryo-EM structure determination. *Nat. Methods* **14**, 290–296 (2017).

55. Zivanov, J., Nakane, T. & Scheres, S. H. W. A Bayesian approach to beam-induced motion correction in cryo-EM single-particle analysis. *IUCrJ* **6**, 5–17 (2019).

56. Emsley, P. & Cowtan, K. Coot: model-building tools for molecular graphics. *Acta Crystallogr. D. Biol. Crystallogr.* **60**, 2126–2132 (2004).

57. Afonine, P. V. et al. New tools for the analysis and validation of cryo-EM maps and atomic models. *Acta Crystallogr. D. Struct. Biol.* **74**, 814–840 (2018).

58. Goddard, T. D. et al. UCSF ChimeraX: meeting modern challenges in visualization and analysis. *Protein Sci.* **27**, 14–25 (2018).

59. Chovancova, E. et al. CAVER 3.0: a tool for the analysis of transport pathways in dynamic protein structures. *PLoS Comput. Biol.* **8**, e1002708 (2012).

60. Smart, O. S., Neduvilil, J. G., Wang, X., Wallace, B. A. & Sansom, M. S. P. HOLE: a program for the analysis of the pore dimensions of ion channel structural models. *J. Mol. Graph.* **14**, 354–360 (1996).

61. Lee, J. et al. CHARMM-GUI Input Generator for NAMD, GROMACS, AMBER, OpenMM, and CHARMM/OpenMM simulations using the CHARMM36 additive force field. *J. Chem. Theory Comput.* **12**, 405–413 (2016).

62. Schrödinger, L. *The {PyMOL} Molecular Graphics System, Version-2.3.* (2015).

63. Lomize, M. A., Pogozheva, I. D., Joo, H., Mosberg, H. I. & Lomize, A. L. OPM database and PPM web server: resources for positioning of proteins in membranes. *Nucleic Acids Res.* **40**, D370–D376 (2012).

64. Huang, J. et al. CHARMM36m: an improved force field for folded and intrinsically disordered proteins. *Nat. Methods* **14**, 71–73 (2017).

65. Kim, S. et al. CHARMM-GUI ligand reader and modeler for CHARMM force field generation of small molecules. *J. Comput. Chem.* **38**, 1879–1886 (2017).

66. Hess, B., Bekker, H., Berendsen, H. J. C. & Fraaije, J. G. E. M. LINCS: A linear constraint solver for molecular simulations. *J. Comput. Chem.* **18**, 1463–1472 (1997).

67. Abraham, M. J. et al. GROMACS: High performance molecular simulations through multi-level parallelism from laptops to supercomputers. *SoftwareX* **1–2**, 19–25 (2015).

Acknowledgements

We thank members of the Du & Lü Labs for thoughtful discussions. Cryo-EM data were collected at the David Van Andel Advanced Cryo-Electron Microscopy Suite and cryo-EM core facility of Northwestern University. We thank G. Zhao and X. Meng for support with data collection at the David Van Andel Advanced Cryo-Electron Microscopy Suite. We appreciate the high-performance computing team of Van Andel Institute, the Structural Biology Facility and Quest High-Performance Computing Cluster at Northwestern University for computational support. W.L. is supported by National Institutes of Health (NIH) grants (R01HL153219, R01NS112363 and R35GM138321). J.D. is supported by a McKnight Scholar Award, a Klingenstein-Simon Scholar Award, a Sloan Research Fellowship in neuroscience, a Pew Scholar in the Biomedical

Sciences award, and NIH grants (R01NS111031 and R01NS129804). Z.R. was supported by American Heart Association postdoctoral fellowship (20POST35120556) and an NIH grant (R01NS128258).

Author contributions

W.L. and J.D. supervised the project. Z.R. and Y.L. generated PANX1 mutants and tested their expression. Y.L. and Z.R. carried out the protein purification, cryo-EM data collection and processing. I.O. and J.L. performed electrophysiological experiments. Y.L., Z.R., J.D. and W.L. analyzed the structures. Z.R., Y.L., E.Z., J.D. and W.L. contributed to manuscript preparation.

Competing interests

Authors declare that they have no competing interests.

Additional information

Supplementary information The online version contains supplementary material available at <https://doi.org/10.1038/s41467-025-66028-9>.

Correspondence and requests for materials should be addressed to Juan Du or Wei Lü.

Peer review information *Nature Communications* thanks the anonymous reviewers for their contribution to the peer review of this work. A peer review file is available.

Reprints and permissions information is available at <http://www.nature.com/reprints>

Publisher's note Springer Nature remains neutral with regard to jurisdictional claims in published maps and institutional affiliations.

Open Access This article is licensed under a Creative Commons Attribution-NonCommercial-NoDerivatives 4.0 International License, which permits any non-commercial use, sharing, distribution and reproduction in any medium or format, as long as you give appropriate credit to the original author(s) and the source, provide a link to the Creative Commons licence, and indicate if you modified the licensed material. You do not have permission under this licence to share adapted material derived from this article or parts of it. The images or other third party material in this article are included in the article's Creative Commons licence, unless indicated otherwise in a credit line to the material. If material is not included in the article's Creative Commons licence and your intended use is not permitted by statutory regulation or exceeds the permitted use, you will need to obtain permission directly from the copyright holder. To view a copy of this licence, visit <http://creativecommons.org/licenses/by-nc-nd/4.0/>.

© The Author(s) 2025